

# Low-luminosity supernovae: SN 2005cs and SN 2020cxd as very low-energy iron core-collapse explosions

Alexandra Kozyreva<sup>1,2\*</sup>, Hans-Thomas Janka<sup>1</sup>, Daniel Kresse<sup>1,3</sup>, Stefan Taubenberger<sup>1</sup>

<sup>1</sup>Max-Planck-Institut für Astrophysik, Karl-Schwarzschild-Str. 1, 85748 Garching, Germany,

<sup>2</sup>Alexander von Humboldt Fellow

<sup>3</sup>Physik-Department, Technische Universität München, James-Frank-Str. 1, 85748 Garching, Germany

Accepted XXX. Received YYY; in original form ZZZ

## ABSTRACT

SN 2020cxd is a representative of the family of low-energy, underluminous Type IIP supernovae (SNe), whose observations and analysis were recently reported by Yang et al. (2021). Here we re-evaluate the observational data for the diagnostic SN properties by employing the hydrodynamic explosion model of a  $9 M_{\odot}$  red supergiant progenitor with an iron core and a pre-collapse mass of  $8.75 M_{\odot}$ . The explosion of the star was obtained by the neutrino-driven mechanism in a fully self-consistent simulation in three dimensions (3D). Multi-band light curves and photospheric velocities for the plateau phase are computed with the one-dimensional radiation-hydrodynamics code STELLA, applied to the spherically averaged 3D explosion model as well as spherisized radial profiles in different directions of the 3D model. We find that the overall evolution of the bolometric light curve, duration of the plateau phase, and basic properties of the multi-band emission can be well reproduced by our SN model with its explosion energy of only  $0.7 \times 10^{50}$  erg and an ejecta mass of  $7.4 M_{\odot}$ . These values are considerably lower than the previously reported numbers, but they are compatible with those needed to explain the fundamental observational properties of the prototype low-luminosity SN 2005cs. Because of the good compatibility of our photospheric velocities with line velocities determined for SN 2005cs, we conclude that the line velocities of SN 2020cxd are probably overestimated by up to a factor of about 3. The evolution of the line velocities of SN 2005cs compared to photospheric velocities in different explosion directions might point to intrinsic asymmetries in the SN ejecta.

**Key words:** supernovae: general - supernovae: individual: SN2005cs: supernovae: individual: SN2020cxd – supernovae – stars: massive – radiative transfer

## 1 MOTIVATION

The recently discovered supernova (SN) 2020cxd is a low-luminosity hydrogen-rich Type II SN (Yang et al. 2021). Due to its low plateau luminosity of about  $10^{41}$  erg s<sup>-1</sup> and relatively low photospheric velocity at the end of the plateau, it is considered as a member of the family of low-luminosity SNe (Pastorello et al. 2009; Spiro et al. 2014; Reguitti et al. 2021). Analysing the bolometric light curve, Yang et al. (2021) inferred the explosion of a red supergiant ( $187 R_{\odot}$ ) with a pre-collapse mass of about  $11 M_{\odot}$  (and a zero-age main sequence (ZAMS) mass of about  $12 M_{\odot}$ ) and an energy of  $0.58 \text{ foe}^1$  ( $1 \text{ foe} = 10^{51}$  erg). SN 2020cxd exhibits a large drop between plateau and the radioactive tail, as well as a very low tail luminosity. The total mass of the ejected radioactive nickel  $^{56}\text{Ni}$  is  $0.003 M_{\odot}$ .

According to the current understanding, based on recent self-

consistent 3-dimensional (3D) simulations of the underlying mechanism that causes the explosion of massive stars, SNe with a plateau in their light curves result from the neutrino-driven mechanism (e.g., Takiwaki et al. 2014; Lentz et al. 2015; Melson et al. 2015a,b; Müller et al. 2017a, 2018; Ott et al. 2018; Summa et al. 2018; Burrows et al. 2019; Glas et al. 2019; Stockinger et al. 2020; Bollig et al. 2021). The amount of radioactive nickel  $^{56}\text{Ni}$  produced in this kind of explosion is proportional to the neutrino luminosity and amount of ejecta material heated by neutrinos. The higher the neutron-star mass (correlated with the progenitor’s compactness as defined by O’Connor & Ott 2011) the higher the neutrino luminosity, the bigger the amount of neutrino-heated ejecta, the more energetic the shock wave, and the larger the mass of radioactive nickel (Nakamura et al. 2015; Ertl et al. 2016; Müller et al. 2016; Sukhbold et al. 2016; Janka 2017; Ertl et al. 2020). These dependencies associated with neutrino-driven explosions are in line with correlations between SN energies,  $^{56}\text{Ni}$  masses and plateau luminosities deduced from observations (Pejcha & Prieto 2015a; Müller et al. 2017b; Pejcha 2020). Recent studies show that the reference amount

\* E-mail: sasha@mpa-garching.mpg.de

<sup>1</sup> The authors report a kinetic energy of 0.43 foe and a thermal energy of 0.15 foe, which results in a total energy of 0.58 foe.

of ejected radioactive nickel  $^{56}\text{Ni}$  is about  $0.03 M_{\odot}$  for a diagnostic explosion energy around 0.6 foe (Müller et al. 2016, 2017a; Ertl et al. 2020). Therefore, the parameters of SN 2020cxid diagnosed by Yang et al. (2021) are in conflict with our current theoretical and observational picture of the underlying physics of core-collapse SN explosions. Motivated by this fact we present here a revision of the analysis made by Yang et al. (2021) with the effort to find a more reliable interpretation for the progenitor of SN 2020cxid and its explosion. We also choose SN 2005cs as a representative member of the family of low-luminosity SNe, because SN 2005cs has a better data coverage, and analyse SN 2020cxid together with SN 2005cs in the context of our theoretical model.

In Section 2 we describe our considered SN model and the radiation-hydrodynamics treatment with the STELLA code. In Section 3 we present bolometric and multi-band light curves as well as photospheric velocities of our model calculations in comparison to observational data for SN 2020cxid and SN 2005cs, including an assessment of the line velocities reported for SN 2020cxid in the literature. In Section 4 we summarize our results and draw conclusions. Appendices A, B, and C present angle-averaged and direction dependent profiles for our considered 3D SN model and corresponding multi-band light curves.

## 2 INPUT MODEL AND METHOD

In Table 1, we report the published properties of SN 2005cs as a representative member of the family of low-luminosity SNe and of the low-luminosity SN 2020cxid, and confront them with the properties of our theoretical model. We consider a star near the low-mass end of SN progenitors with an initial mass of  $9 M_{\odot}$  (Sukhbold et al. 2016) as the most suitable model. A low-energy neutrino-driven explosion of such a low-mass progenitor can explain low-luminosity SNe, as was already discussed by a number of observational and theoretical studies (Mattila et al. 2008; Van Dyk et al. 2012; Jerkstrand et al. 2018). We note that the study by Utrobin & Chugai (2008) explains SN 2005cs with an explosion of a higher-mass progenitor of  $18.2 M_{\odot}$ , however, their study was based on a non-evolutionary progenitor configuration. A connection with the explosion of such a high-mass progenitor, however, is disfavoured by recent self-consistent 3D models of neutrino-driven explosions of  $18-19 M_{\odot}$  stars (Müller et al. 2017a; Bollig et al. 2021).

Our progenitor model of a star with an initial mass of  $9 M_{\odot}$  (model s9.0 of Sukhbold et al. 2016) was computed with the stellar evolution code KEPLER (Weaver et al. 1978) until the onset of iron-core collapse (Woosley & Heger 2015). A one-dimensional (1D) SN simulation of this model, which was exploded parametrically via neutrino heating by Ertl et al. (2016) and Sukhbold et al. (2016), led to an explosion energy of 0.11 foe. This explosion model was later used for nebular spectral modeling by Jerkstrand et al. (2018). The corresponding self-consistent 3D simulation of a neutrino-driven explosion of this  $9 M_{\odot}$  progenitor model with the PROMETHEUS-VERTEX code was first discussed in Melson et al. (2020) and was later used for long-time 3D simulations with PROMETHEUS-HOTB by Stockinger et al. (2020). Independently, the s9.0 model was successfully exploded in 3D by Glas et al. (2019) and by Burrows et al. (2019).

For our present work we use the s9.0 model of Stockinger et al. (2020), which has already been used as input for the study by Kozyreva et al. (2021). We note that an improved post-processing analysis is applied in the present work and the profiles are extracted from the 3D simulation at an earlier epoch, namely at 1.974 days

after core collapse. At this moment the fastest parts of the shock are within 0.2 days before their breakout from the stellar surface. The shock front is strongly deformed, and the slowest parts of the shock reach the stellar surface only approximately 1 day later, i.e. about 3.1 days after the onset of the explosion. In Appendix A, we present comparative plots showing the structure of the angle-averaged profiles used in Kozyreva et al. (2021) compared to the profiles used as input in the present work. The geometry of the shock front is far from spherical symmetry and the distribution of the ejected  $^{56}\text{Ni}$  displays a main plume and a few smaller plumes of high-entropy material. We illustrate the asphericity of the model in Figure 1. In total we extract 16 radial profiles which represent the structure of the ejecta in different angular directions of the 3D model. The profiles are listed in Table 2 and are named according to the angle relative to the central-axis direction of the fastest plume of the ejected  $^{56}\text{Ni}$  (see Figure 1). The density and velocity profiles along with the distribution of the  $^{56}\text{Ni}$  mass fraction in each of the different radial directions are shown in Appendix B. We note that the value of the explosion energy of  $0.48 \times 10^{50}$  erg as given in Table 4 of Stockinger et al. (2020) is taken at the end of the PROMETHEUS-VERTEX simulation at 3.14 s, whereas we give the value at 1.974 days from the long-time continuation run with the PROMETHEUS-HOTB code.

In the current study, the 3D explosion model is mapped into the 1D radiation-hydrodynamics code STELLA (Blinnikov et al. 2006). STELLA is capable of processing hydrodynamics as well as the radiation field evolution, i.e. computing light curves, spectral energy distribution and resulting broad-band magnitudes and colours. We use the standard parameter settings, well-explained in many papers involving STELLA simulations (see e.g., Kozyreva et al. 2019; Moriya et al. 2020). The thermalisation parameter is set to 0.9 as recommended by the recent study of Kozyreva et al. (2020). The profiles along different radial directions are spherisized during the mapping into STELLA. The corresponding  $4\pi$ -equivalent values of different quantities are listed in Table 2. The total amount of  $^{56}\text{Ni}$  is scaled to  $0.003 M_{\odot}$  to match the mass of  $^{56}\text{Ni}$  estimated for SN 2020cxid (Yang et al. 2021). A value of the  $^{56}\text{Ni}$  (plus  $^{56}\text{Co}$  and  $^{56}\text{Fe}$ ) yield of  $0.00635 M_{\odot}$  was reported by Stockinger et al. (2020) for the 3D explosion model of s9.0 and recently determined to be  $0.0057 M_{\odot}$  by a more accurate re-evaluation of the simulation outputs (see data in <https://wwwmpa.mpa-garching.mpg.de/ccsnarchive/data/Stockinger2020/>). Note that the angle-averaged profile in Kozyreva et al. (2021) had  $0.005 M_{\odot}$  of  $^{56}\text{Ni}$ . We mention two reasons why a rescaling of the  $^{56}\text{Ni}$  mass is well motivated:

(i) The nucleosynthesis calculations yielding the values reported by Stockinger et al. (2020) and re-evaluated in the present study were only approximate, because they were based on the use of a small nuclear  $\alpha$ -chain network.

(ii) The exact amount of  $^{56}\text{Ni}$  produced in 3D explosion models is extremely sensitive to the electron fraction ( $Y_e$ ) in the neutrino-heated ejecta, which is determined by the interaction of the innermost ejecta with the intense neutrino radiation from the proto-neutron star. Therefore, the  $Y_e$  distribution in these ejecta depends sensitively on the details of the neutrino physics and neutrino transport, including the still incompletely understood effects of neutrino-flavor oscillations in and near the proto-neutron star.

The uncertainties in the exact ejected mass of  $^{56}\text{Ni}$  corresponding to these points can well amount to a factor of 2.

Recently, radiative transfer simulations with the spherically averaged 3D explosion model of s9.0 were done in a separate paper and compared to the low-luminosity SNe 2005cs and 1999br (Kozyreva et al. 2021). The model matches the broad-band mag-

**Table 1.** Parameters of the low-luminosity SNe 2020cxd, 2005cs, and the angle-averaged parameters of model s9.0.  $t_p$  is the duration of plateau phase which ends at the middle of the transition to the radioactive tail. Radius is the progenitor radius at the pre-collapse stage. Uph is the photospheric velocity around the middle of the plateau measured via the  $H\alpha$  line.

SN	$M_{\text{bol}}$ [mags]	$t_p$ [days]	Uph [1000 km s $^{-1}$ ]	Radius [ $R_{\odot}$ ]	$M_{\text{ej}}$ [ $M_{\odot}$ ]	$M_{\text{prog}}$ [ $M_{\odot}$ ]	$M_{56\text{Ni}}$ [ $M_{\odot}$ ]	$E_{\text{expl}}$ foe	Reference
2020cxd	-14.0	130	4	187	9.5		0.003	0.58	Yang et al. (2021)
2005cs	-14.58	130	1.5	100	11.1		0.0028	0.3	Pastorello et al. (2009)
				357	9.5		0.006	0.16	Pumo et al. (2017)
				600	15.9	18.2	0.0082	0.41	Utrobin & Chugai (2008)
s9.0				408	7.4	8.75	0.003	0.068	present study

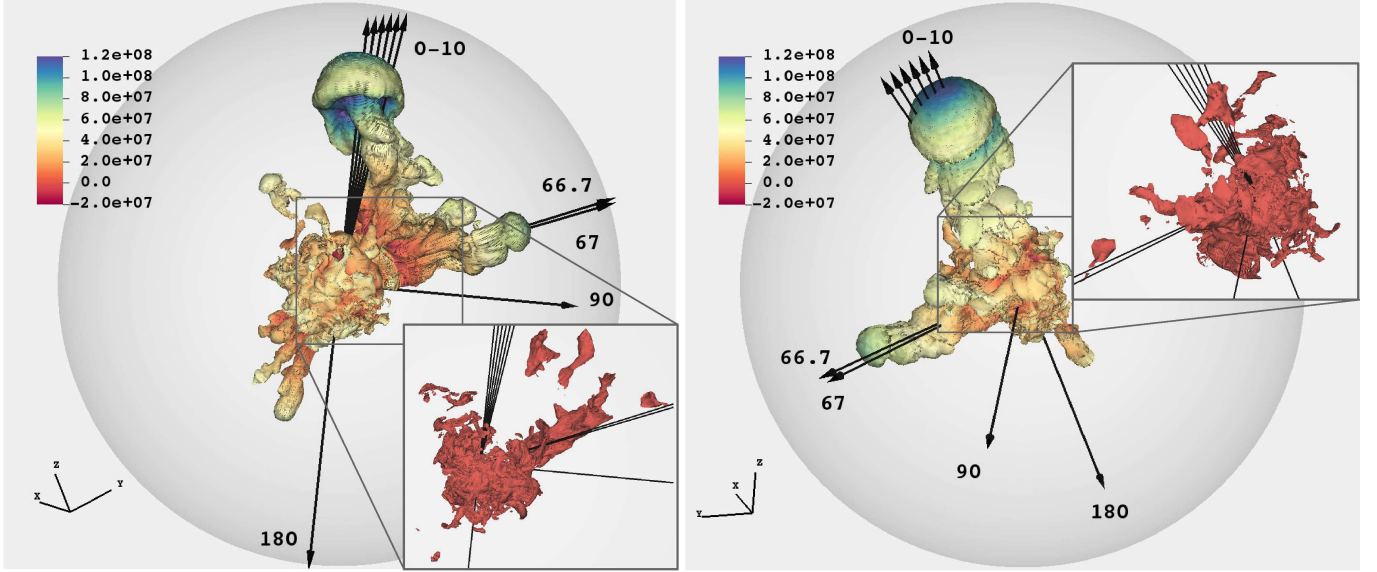


**Figure 1.** Three-dimensional explosion geometry of the s9.0 model (Stockinger et al. 2020) used as input for the present study. The two panels show different views of the isosurface of a constant  $^{56}\text{Ni}$  mass fraction of 0.01 at 1.974 days after core collapse ( $\sim 0.2$  days before the fastest part of the deformed SN shock reaches the stellar surface), with the radial velocity (in units of  $\text{cm s}^{-1}$ ) colour-coded. The zoom insets show the isosurface of a constant  $^{56}\text{Ni}$  mass fraction of 0.1 with the same colour-coding. The semi-transparent grey sphere marks the stellar surface (at a radius of  $2.86 \times 10^{13}$  cm). Black arrows denote the selected angular directions as listed in Table 2; for reasons of clarity we do not show the “-” directions (i.e.,  $-2^\circ$  to  $-10^\circ$ ), which are distinguished from the “+” directions ( $+2^\circ$  to  $+10^\circ$ ) by an azimuthal angular shift of  $180^\circ$  around the major  $^{56}\text{Ni}$  plume axis (i.e., the  $0^\circ$  direction).

nitides and bolometric light curves of these observed SNe. The comparison demonstrates the applicability of the given model for low-luminosity SNe. Hence, it has already been shown that our explosion model of the  $9 M_{\odot}$  progenitor is capable of explaining a number of members of the family of low-luminosity SNe.

### 3 RESULTS

#### 3.1 Bolometric properties

In Figure 2 bolometric light curves for different radial directions of our 3D explosion simulation and the angle-averaged case of model s9.0 are displayed. We superpose bolometric light curves of two low-luminosity SNe, SN 2020cxd and SN 2005cs. Our  $66.7^\circ$ ,  $90^\circ$ ,  $180^\circ$ , and angle-averaged cases are capable of matching the bolometric light curve of SN 2020cxd to a very large extent without any artificial tuning besides a proper scaling of the  $^{56}\text{Ni}$  mass to match the observationally determined value (see Section 2). And they are

also able to reproduce the global behaviour of the bolometric light curve of SN 2005cs.

Because the explosion energy is a crucial factor governing the plateau luminosity (Arnett 1980; Popov 1993; Kasen & Woosley 2009; Sukhbold et al. 2016; Goldberg et al. 2019; Kozyreva et al. 2019), a luminosity of a Type IIP SN as low as  $L \simeq 10^{41}$  erg s $^{-1}$  or  $-14$  mags (average for the low-luminosity family) can be reproduced by very low explosion energies, around or below 0.1 foe for stars near the low-mass end of core-collapse SN progenitors (Pumo et al. 2017). The  $V$ -band magnitude ( $V$ ) and the bolometric luminosity ( $L$ ) at the middle of the plateau are:

$$\begin{aligned} V &\sim 1.25 \log M - 2.08 \log E - 1.67 \log R, \\ \log L &\sim -0.4 \log M + 0.74 \log E + 0.76 \log R, \end{aligned} \quad (1)$$

where  $M$  is the ejecta mass,  $E$  the explosion energy, and  $R$  the progenitor radius prior to the explosion. The scaling relations are taken from Popov (1993) and Goldberg et al. (2019), respectively. Note that we neglect the additive terms given in these references, because we are only interested in the dependencies. If the energy varies between 0.03 foe and 1.5 foe (Ertl et al. 2016; Stockinger et al. 2020), this

**Table 2.** Isotropic-equivalent parameter values for the profiles corresponding to different radial directions and for the angle-averaged profile (labeled “< .. >”) taken from the 3D model s9.0 (Stockinger et al. 2020). The name of the direction represents the angle from the axis of the main high-entropy plume. For the cases of  $2^\circ$ – $10^\circ$  we show two (“+” and “-”) directions, which are distinguished by an azimuthal angular shift of  $180^\circ$  around the axis of the major  $^{56}\text{Ni}$  plume (i.e., the  $0^\circ$  direction). The total mass of radioactive  $^{56}\text{Ni}$  is a sum of  $^{56}\text{Ni}$  and its daughter products  $^{56}\text{Co}$  and  $^{56}\text{Fe}$ . Note that we list the  $^{56}\text{Ni}$  mass ( $M_{56\text{Ni}}$ ) with the value that is present in each of the profiles before scaling to  $0.003 M_\odot$  needed to match the mass of  $^{56}\text{Ni}$  in SN 2020cx and SN 2005cs.  $M_{\text{tot}}$  is the isotropic-equivalent total mass including the central compact object, while  $M_{\text{ej}}$  is the isotropic equivalent of the ejected mass.  $E_{\text{expl}}$  is the  $4\pi$ -equivalent explosion energy at 1.974 days.  $E_{\text{kin}}$  is the analogously determined terminal kinetic energy at the end of the radiative transfer simulations (at day 170), before and after scaling the  $^{56}\text{Ni}$  mass to  $0.003 M_\odot$ . The energy difference is a consequence of the different release of energy in radioactive  $^{56}\text{Ni}$  and  $^{56}\text{Co}$  decay which contributes to the energy balance after the energies of  $\gamma$ -rays and positrons are thermalised.

direction	$M_{56\text{Ni}}$ [ $M_\odot$ ]	$M_{\text{tot}}$ [ $M_\odot$ ]	$M_{\text{ej}}$ [ $M_\odot$ ]	$E_{\text{expl}}$ [ $10^{50}$ erg]	$E/M$ [foe/ $M_\odot$ ]	$E_{\text{kin}}$ [ $10^{50}$ erg]
$0^\circ$	0.0974	5.75	4.40	1.2812	0.0303	1.3337/1.2641
$+2^\circ$	0.0886	5.96	4.61	1.3069	0.0293	1.3502/1.2915
$-2^\circ$	0.0951	5.48	4.13	1.1885	0.0299	1.2362/1.1701
$+4^\circ$	0.1229	6.14	4.79	1.2964	0.0286	1.3684/1.2801
$-4^\circ$	0.1150	5.70	4.35	1.1553	0.0278	1.2110/1.1289
$+6^\circ$	0.1278	6.23	4.88	1.1894	0.0259	1.2626/1.1641
$-6^\circ$	0.0947	5.79	4.44	1.0850	0.0253	1.1233/1.0543
$+8^\circ$	0.0947	6.38	5.03	1.0524	0.0217	1.0931/1.0177
$-8^\circ$	0.0540	5.85	4.50	0.9425	0.0210	0.9459/0.9070
$+10^\circ$	0.0814	6.50	5.15	0.8836	0.0177	0.9122/0.8445
$-10^\circ$	0.0460	6.12	4.77	0.7960	0.0166	0.7930/0.7583
$66.7^\circ$	0.0659	8.68	7.32	0.8026	0.0117	0.8594/0.7951
$67^\circ$	0.0582	8.66	7.31	0.8030	0.0117	0.8523/0.7964
$90^\circ$	0.0010	8.75	7.40	0.7596	0.0102	0.7524/0.7544
$180^\circ$	0.0026	8.80	7.45	0.6943	0.0092	0.6884/0.6887
< .. >	0.0057	8.75	7.40	0.7334	0.0095	0.6790/0.6765

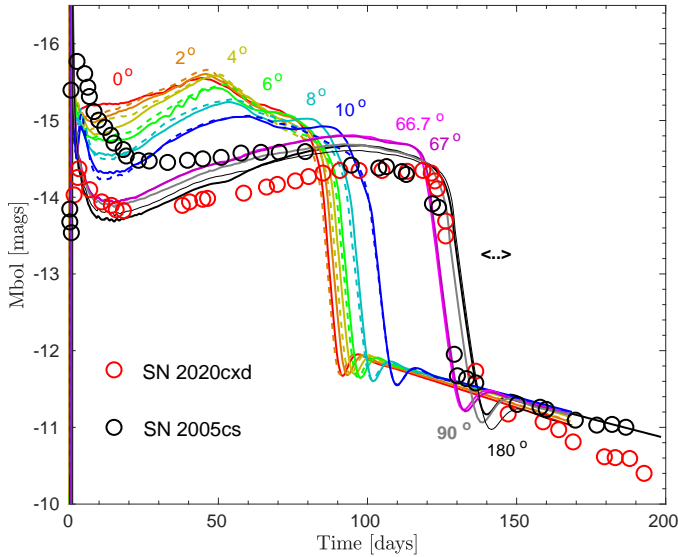


**Figure 2.** Bolometric light curves (in absolute magnitudes) for different radial directions of model s9.0, and low-luminosity SNe 2005cs and 2020cx. The label “< .. >” represents the light curve for the angle-averaged profile. The solid and dashed curves indicate the “+” and “-” directions for the cases of  $2^\circ$ – $10^\circ$ , as introduced in Table 2.

corresponds to  $-1.5$  and  $0.2$  in logarithmic scale, which results in a luminosity scatter up to 1 dex. The low explosion energy required for low-luminosity events can be released in low-mass progenitors of  $9$ – $10 M_\odot$ , as the energy exhibits a (rough) tendency to increase with the initial progenitor mass (Nakamura et al. 2015; Ertl et al. 2016; Müller et al. 2016; Pejcha 2020). The second strongest factor is the

progenitor radius, and the weakest effect is connected to the ejecta mass. The radius ranges between  $100 R_\odot$  and a few  $1000 R_\odot$  for the observed red-supergiants (Levesque et al. 2005, 2006). This leads to a scatter in luminosity of 0.76 dex. The ejecta mass tends to be around  $10 M_\odot$  and has a relatively less important effect. To reach very low luminosities, the radius of the progenitors should not be very large, yet it should still allow for sufficient recombination to power the light curve (Grasberg & Nadezhin 1976) and to provide an extended plateau phase, since shrinking the progenitor radius shortens the duration of the plateau:

$$\begin{aligned} \log t_p &\sim 0.5 \log M - 0.167 \log E + 0.167 \log R, \\ \log t_p &\sim 0.41 \log M - 0.28 \log E - 0.02 \log R + 0.13 \log M_{\text{Ni}}, \end{aligned} \quad (2)$$

where  $t_p$  is the plateau duration,  $M$ ,  $E$ , and  $R$  have the same meaning as in Equation 1, and  $M_{\text{Ni}}$  is the total mass of radioactive  $^{56}\text{Ni}$ . The relations are taken from Popov (1993) and Goldberg et al. (2019), respectively. Note that the updated scaling relation for the plateau duration from Goldberg et al. (2019) do not show strong dependence on the progenitor radius. Even though the highest exponent is in the mass term, the mass does not strongly affect the variations of the duration since the ejecta mass is always close to  $10 M_\odot$ . The influence of radioactive nickel in the ejecta on the plateau luminosity is moderate, in particular, the plateau duration is strongly affected by the presence of nickel and its distribution (Kozyreva et al. 2019). However, for low-mass explosions, which we consider as the most probable explanation for the low-luminosity SNe, the  $^{56}\text{Ni}$  yield is a few thousandths of a solar mass and does not extend the length of the plateau and its luminosity value to any significant extent (see Kozyreva et al. 2021).

The light curves for the directions aligned with the fastest parts of the s9.0 ejecta, i.e. close to the directions of  $0^\circ$  –  $10^\circ$ , do not match

the given observed low-luminosity SNe. Nevertheless, we presume that flux from these angles may contribute to other directions. To clarify the question on the contributions of other radial directions to the particular viewing direction, realistic 3D radiative-transfer simulations are required, which may be carried out in the future.

Interestingly, the bolometric light curve during the plateau increases for SN 2020cxid until shortly before the steep decline to the nickel tail, which is amazingly well reproduced by our explosion model for the angle-averaged profiles and the directions at  $66.7^\circ$ ,  $67^\circ$ ,  $90^\circ$ , and  $180^\circ$ . In contrast, SN 2005cs shows nearly a flat plateau and after the middle of the plateau a shallow decline sets in well before the steep drop to the radioactive tail. Such a difference in the shape of the plateau was discussed in [Kozyreva et al. \(2019\)](#). It could, in principle, be connected to different degrees of mixing of radioactive  $^{56}\text{Ni}$ . In the context of the considered low-luminosity SNe, however, this explanation is disfavored by the small mass of only  $0.003 M_\odot$  of ejected  $^{56}\text{Ni}$  ([Kozyreva et al. 2021](#)).

The different light-curve shapes of SN 2005cs and SN 2020cxid might instead be a hint of a considerable degree of explosion asymmetry in the former case, even already during the shock-breakout phase and during the early expansion of the hydrogen envelope. Such a possibility for SNe of low-mass progenitors is suggested by the extreme deformation of the ejecta associated with the largest nickel plume in our 3D explosion model s9.0. This nickel-rich plume extends through the entire hydrogen envelope and pushes the expansion of the SN shock wave. Therefore, when the head of the plume reaches the stellar surface, the shock breaks out roughly 1 day earlier than in the other directions (see [Stockinger et al. 2020](#) and our discussion in Section 2 connected to Figure 1). The light curves computed for spherized ejecta conditions in different directions of our 3D explosion model (as displayed in Figure 2) suggest the possible influence of such explosion asymmetries. In the directions from  $0^\circ$  to  $10^\circ$  relative to the axis of the biggest nickel-rich plume, the higher explosion energy per solid angle leads to faster expansion of the ejecta and of the photospheric radius and thus lifts the light curve during the initial decline to the plateau and the early phase of the plateau. This might account for the higher luminosity of SN 2005cs during the first 20 days and the flat evolution of its plateau afterwards until about 80–90 days. The luminosity during this phase could therefore be boosted by the emission from faster ejecta for an explosion with considerable asymmetry in the outer hydrogen envelope, whereas SN 2020cxid would not be influenced by such effects, at least not for our viewing direction. At later times during the plateau phase, when the emitted radiation escapes from deeper layers, where the radioactive nickel and ejecta energy are more spherically distributed (see Figure 1), the outer asymmetries play no important role any longer and the light curves become more similar, as seen for SN 2005cs and SN 2020cxid after about 90 days (Figure 2). Of course, based on our 1D radiative transfer modeling such an interpretation remains speculative. It requires confirmation by 3D light-curve calculations for different viewing angles for our 3D explosion model s9.0 or other low-mass 3D SN models with large-scale explosion asymmetries.

### 3.2 Broad-band light curves compared to low-luminosity SNe

We present *UBVR* broad-band light curves for all considered angular directions of our model s9.0 in Appendix C. In this section we show the results for a few selected angular directions suitable to reproduce the light curve properties of low-luminosity SNe 2020cxid and 2005cs (Figure 3 and Figure 4, respectively). In Figure 3, *ugri* magnitudes for the  $90^\circ$ ,  $180^\circ$ , and angle-averaged cases are shown together with those observed in SN 2020cxid. It is difficult to draw conclusions

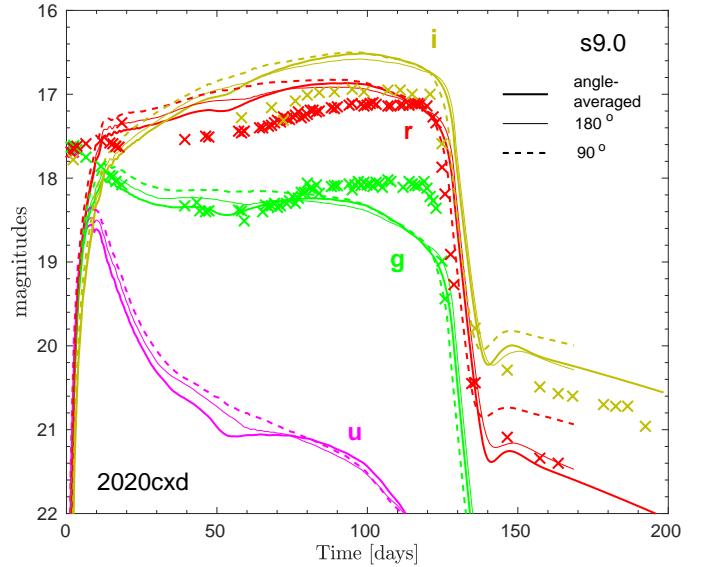


**Figure 3.** *ugri* broad-band light curves (in apparent magnitudes) for selected directions of model s9.0 and SN 2020cxid ([Yang et al. 2021](#)).

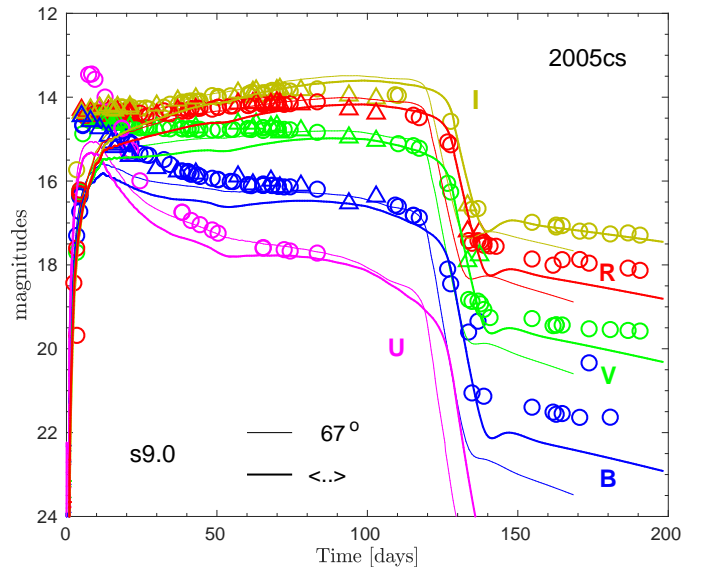


**Figure 4.** *UBVR* broad-band light curves (in apparent magnitudes) for selected directions of model s9.0 and SN 2005cs. The observational data for SN 2005cs are taken from [Tsvetkov et al. \(2006\)](#) (triangles) and from [Pastorello et al. \(2009\)](#) (circles).

about the relevance of the synthetic light curves because of the limited set of filters used for the photometry of SN 2020cxid. However, the general behaviour of the fluxes in broad bands is explained by our selected cases. Specifically, the flux in the *g*-band is reproduced by the directions outside the main plume of s9.0 or the angle-averaged case to good agreement.

At the same time, the  $66.7^\circ$ ,  $67^\circ$ ,  $90^\circ$ ,  $180^\circ$ , and angle-averaged models, match the general behaviour of the broad-band magnitudes of SN 2005cs ([Pastorello et al. 2006](#); [Tsvetkov et al. 2006](#); [Pastorello et al. 2009](#)), except during the first  $\sim 50$  days when the

models underestimate the flux in all bands. However, the same is true for the comparison with the bolometric light curve of SN 2005cs as discussed in Section 3.1. We show only light curves for the  $67^\circ$  and angle-averaged cases, as the rest of the suitable cases range between the  $67^\circ$  and angle-averaged curves.

Nevertheless, we conclude that our angle-averaged model of s9.0 and the directions outside the main plume explain bolometric and broad-band light curves of the considered observational examples of the low-luminosity SN family sufficiently well. This is particularly noteworthy because we do not tune the output of the self-consistent 3D explosion simulations while mapping it into the radiative-transfer code STELLA except for adjusting the  $^{56}\text{Ni}$  mass. We consider the good match between low-luminosity SN observations and our results for the light-curve modeling as a strong support for neutrino-driven explosion models of low-mass, low-energy SN explosions.

### 3.3 Photospheric velocity

One of the distinct observational features of low-luminosity SNe is the relatively low photospheric velocity during the plateau (Pignata 2013; Spiro et al. 2014). A low photospheric velocity ( $U_{\text{ph}}$ ) or, more precisely, a low ratio between energy and ejecta mass (Tomasella et al. 2018), is the strongest diagnostic of low-energy explosions.

#### 3.3.1 Line velocities in SNe 2020cxd and 2005cs

In observations,  $U_{\text{ph}}$  cannot be measured directly, but is usually approximated by measuring the velocity corresponding to the blueshift of the P-Cygni absorption lines. Dessart & Hillier (2005) have shown, based on synthetic spectra, that the so-derived velocities are good proxies for  $U_{\text{ph}}$  in the case of weak lines (such as Fe lines), but that with a strong line such as  $\text{H}\alpha$ ,  $U_{\text{ph}}$  is often overestimated by up to 40%.

For SN 2005cs, Pastorello et al. (2009) have measured  $\text{H}\alpha$  and  $\text{Sc II}$  velocities that are a factor of  $\sim 2$  lower than in normally luminous SNe II, declining from  $\sim 7000 \text{ km s}^{-1}$  in the earliest spectra to  $1000\text{--}1500 \text{ km s}^{-1}$  at the end of the plateau phase. The  $\text{H}\alpha$  velocity evolution determined by Yang et al. (2021) for SN 2020cxd is surprisingly different from that of SN 2005cs, starting off at similar values a few days after the explosion, but declining only to  $\sim 3000 \text{ km s}^{-1}$  at the end of the plateau. However, these results have to be questioned for mainly two reasons:

(i) For epochs later than 100 d, Yang et al. (2021) chose to measure the full width at half maximum (FWHM) of the  $\text{H}\alpha$  emission line rather than the blueshift of the P-Cygni absorption. This renders it difficult to directly compare to values determined from absorption-line blueshifts. But even more, there is also a fundamental problem in the physical interpretation of these numbers. The FWHM of an emission line is a good indicator for the size of the emitting region in fully optically thin conditions, i.e., when no part of the emission is obscured by an optically thick inner core. However, the assumption of such conditions would automatically imply that  $U_{\text{ph}} = 0$ , meaning that FWHM measurements of emission lines are never a good way to measure  $U_{\text{ph}}$ .

(ii) At  $t < 100$  d, three out of four spectra of SN 2020cxd have been obtained with the SED Machine spectrograph on the Palomar 60-inch telescope. The SED Machine has a very low resolving power of  $R = \frac{\lambda}{\Delta\lambda} \approx 100$  (Blagorodnova et al. 2018), corresponding to a velocity resolution of  $\Delta v = c/R \approx 3000 \text{ km s}^{-1}$ . This sets a lower limit for reliably measurable line blueshifts that is significantly

higher than, e.g., the  $\text{H}\alpha$  blueshifts of SN 2005cs towards the end of the plateau. Consequently, at least the  $\text{H}\alpha$  velocity measurement of SN 2020cxd at day 94 ( $\sim 3750 \text{ km s}^{-1}$ ) appears dubious.

To assess the possible effect of the SED Machine’s low resolution more quantitatively, we artificially degrade the resolution of a 92 d spectrum of SN 2005cs (Faran et al. 2014) to yield  $R \approx 100$  by boxcar-smoothing it with a kernel of  $\sim 65 \text{ \AA}$  and rebinning it to  $25 \text{ \AA}$  bins. In Figure 5 we present the result of this procedure and demonstrate the corresponding effect of the low spectral resolution on estimating the photospheric expansion velocities via the  $\text{H}\alpha$  line as in Yang et al. (2021). Panel (a) shows the spectrum of SN 2005cs taken 94 d after the explosion with the KAST spectrograph (Faran et al. 2014). The  $\text{H}\alpha$  and  $\text{Ba II}$  lines are rather narrow and well separated. A reliable  $\text{H}\alpha$  velocity can be determined. Panel (b) displays the same spectrum, but artificially degraded to match the resolution of SED Machine ( $R \sim 100$ ; Blagorodnova et al. 2018) at a bin width of  $25 \text{ \AA}$ . The  $\text{H}\alpha$  and  $\text{Ba II}$  lines are fully blended, and the velocity inferred from the combined absorption trough is several times higher. Panel (c) presents a comparison between the temporal  $\text{H}\alpha$  velocity evolution of SN 2005cs measured in the original spectra (Pastorello et al. 2009; Faran et al. 2014) and that determined from simulated spectra with SED Machine-like resolution.

In the well-resolved original spectrum, for example, we measure an  $\text{H}\alpha$  velocity of  $\sim 1150 \text{ km s}^{-1}$ , in good agreement with the velocity evolution shown in Pastorello et al. (2009). In the smoothed spectrum, however, the  $\text{H}\alpha$  line is completely blended with several  $\text{Ba II}$  lines at slightly shorter wavelengths, and an attempt to measure the blueshift of the resulting trough yields an alleged  $\text{H}\alpha$  velocity of  $\sim 5100 \text{ km s}^{-1}$ . If the same  $\text{Ba II}$  lines also contribute to the 94 d spectrum of SN 2020cxd, the reported  $\text{H}\alpha$  velocity is likely to be overestimated by a factor of several.

In conclusion, the only line-velocity measurements of SN 2020cxd that can serve to estimate a photospheric velocity are those at  $< 10$  d after explosion, where the velocities are high enough that the low resolution of the SED Machine changes the result by at most a few hundred  $\text{km s}^{-1}$ .

#### 3.3.2 Modelled photospheric velocities

Figure 6 displays the photospheric velocity evolution for our set of different radial directions from the asymmetric 3D explosion model s9.0. The photospheric velocity in STELLA is estimated as the velocity of the shell where the integrated optical depth in the  $B$ -band is equal to  $2/3$ . We superpose the data for the  $\text{H}\alpha$  velocities of SN 2020cxd and SN 2005cs, and the  $\text{Sc II}$  velocities of SN 2005cs. The velocity evolution estimated via the observed  $\text{H}\alpha$  line in SN 2020cxd (Yang et al. 2021) as well as in SN 2005cs (Pastorello et al. 2009) is displayed after dividing the reported observational data by 1.4. This is considered as a proxy to the photospheric velocity, because Dessart & Hillier (2005) showed that the  $\text{H}\alpha$  velocity exceeds the photospheric velocity by a factor of  $0.8\text{--}1.4$ , whereas the velocity of the Fe 5169  $\text{\AA}$  line is a good representation of the photospheric velocity. Nevertheless, even after dividing by 1.4, the  $\text{H}\alpha$  velocity for SN 2020cxd remains too high compared to the values typically found for the family of low-luminosity SNe.

The photospheric velocity evolution for all explored radial directions is shown in Figure 6, because we presume that depending on the viewing direction of the SN, intrinsic, large-scale explosion asymmetries of low-mass iron-core progenitors as suggested by our explosion model s9.0 from Stockinger et al. (2020) may have some influence on the observed line velocities, in addition to their possible effects on

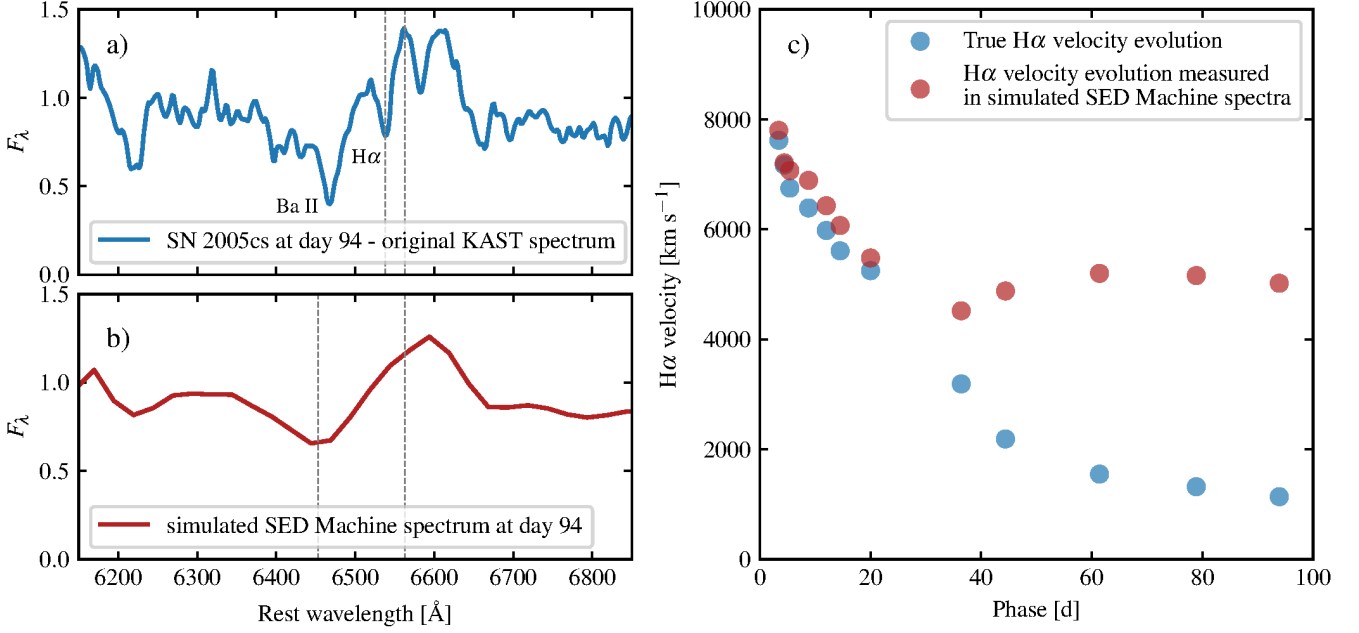


**Figure 5.** Demonstration of the effect of the spectral resolution on the measurement of line velocities. (a) Spectrum of SN 2005cs at 94 d (Faran et al. 2014); (b) its artificially degraded analogue mimicking the resolution of the P60 spectrograph, and (c) H $\alpha$  velocities deduced from the original spectra compared to those derived from their simulated low-resolution counterparts.

the light curve discussed in Section 3.1. Therefore, since our analysis is based on 1D radiative transfer instead of full 3D transport calculations, it may be informative to consider the variation of the photospheric velocities in the different radial directions.

The spectral observations are sparse and under-resolved during the plateau phase of SN 2020cx, as discussed in Section 3.3.1, which calls the information available for the photospheric velocity into question. Most of the spectra were taken with the SED Machine on the P60 telescope, which is a spectrograph with low spectral resolution. The low spectral resolution affects ejecta-velocity estimates. This is especially true for the velocities at day 2.4, day 7.5, and day 94.4, all of which are probably too high. Moreover, a comparison of the H $\alpha$  velocities to the photospheric velocity estimated in STELLA has to be taken with caution, because the synthetic velocity estimate relies on the optical depth in the  $B$ -band and corresponds to the velocity measured via iron and scandium spectral lines, e.g., Fe 5169  $\text{\AA}$  or Sc 6246  $\text{\AA}$ . Assuming the H $\alpha$  velocity is correct and represents the location of the photosphere, the corresponding explosion energy of SN 2020cx would be about  $1.5 \text{ foe}^2$ , which is very high even for a canonical Type IIP SN. Assuming the H $\alpha$  velocity is two times higher than the realistic photospheric velocity (which may be too large a reduction), the explosion energy is still  $0.5 \text{ foe}$ , which corresponds to the average explosion energy of core-collapse SNe.

Nevertheless, the spectral lines remain quite narrow later, if we ignore the resolution constraints of the spectra, and at day 240 the measured intrinsic FWHM of the H $\alpha$  line is only  $478 \text{ km s}^{-1}$ . Nebular spectral synthesis for the 1D version of model s9.0 displays narrow lines with FWHM about  $1000 \text{ km s}^{-1}$  at a similar epoch (Jerkstrand et al. 2018), corresponding to an explosion energy of

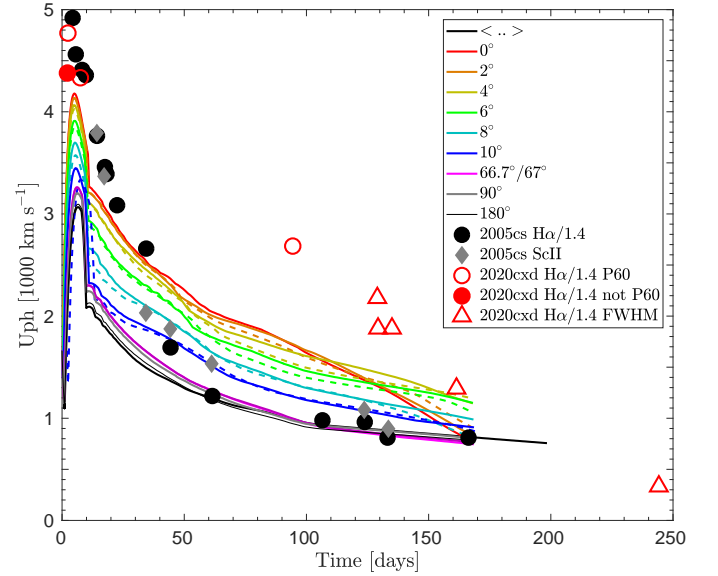


**Figure 6.** Time evolution of the photospheric velocity,  $U_{\text{ph}}$ , for different radial directions of model s9.0. The label  $\langle \dots \rangle$  corresponds to the angle-averaged profile. The solid and dashed curves indicate the “+” and “−” directions for the cases of  $2^\circ$ – $10^\circ$ , as introduced in Table 2. The data points for SN 2005cs are taken from Pastorello et al. (2009) and those for SN 2020cx are taken from Yang et al. (2021). The H $\alpha$  velocity data are plotted after dividing by a factor of 1.4. The reliable data points are shown as filled symbols, whereas the open symbols represent less reliably measured velocities. See explanation in the text.

<sup>2</sup> Assuming the ejecta mass of  $9.5 M_\odot$  and photospheric velocity of  $4000 \text{ km s}^{-1}$ , the diagnostic energy is  $M \times v^2/2 \simeq 1.5 \times 10^{51} \text{ erg}$ .

0.11 foe of the underlying 1D explosion model of s9.0 from [Ertl et al. \(2016\)](#) and [Sukhbold et al. \(2016\)](#). The very low velocity of SN 2020cxcd at day 240 might be explained by an even lower explosion energy. Note that the 1D SN model of s9.0, which was exploded by a parametric treatment of the neutrino-heating mechanism ([Ertl et al. 2016](#); [Sukhbold et al. 2016](#)), releases 0.11 foe, whereas the angle-averaged model of the self-consistent 3D neutrino-driven explosion simulation ([Stockinger et al. 2020](#)) has 0.07 foe. This corresponds to a factor of 0.8 in velocity, which is consistent with the observationally diagnosed ejecta velocity of SN 2020cxcd after about 200 days to some extent.

None of the model results for the different angular directions of the 3D explosion of s9.0 can explain the photospheric velocity evolution of SN 2020cxcd by itself. In fact, the  $H\alpha$  velocities of SN 2020cxcd around 100–150 days exceed the photospheric velocities of all model directions by far. Taking into account the discussion above and in the previous Section 3.3.1, we compare the synthetic velocities also to the more reliable data for the low-luminosity SN 2005cs. The photospheric velocity evolution of SN 2005cs is estimated via the Sc II line ([Pastorello et al. 2009](#)). In contrast to SN 2020cxcd, the line velocities of SN 2005cs are close to our computed results or overlap with them. During the plateau we can explain the photospheric velocity evolution of SN 2005cs with the velocities for the  $8^\circ$  and  $10^\circ$  directions, while at the end of the plateau and later our model directions for  $66.7^\circ$ ,  $67^\circ$ ,  $90^\circ$ ,  $180^\circ$ , as well as the angle-averaged case match the observed values. However, we note that the photospheric velocity estimates beyond the plateau phase are not perfectly reliable in the simulations carried out with STELLA, because STELLA is not capable to provide photospheric information when the SN ejecta become semi-transparent.

The fact that the evolution of the observationally diagnosed photospheric velocity of SN 2005cs agrees with the photosphere of our explosion model in different radial directions at different times during the plateau on the one hand and with the angle-averaged model at the end of the plateau on the other hand, might indicate some influence of explosion asymmetries on the line formation. This interpretation is compatible with our arguments for a possible impact of explosion asymmetries on the light curve of SN 2005cs discussed in Section 3.1. Such explosion asymmetries, which are suggested by the low-mass iron-core explosion model s9.0 of [Stockinger et al. \(2020\)](#), might play a role also in SN 2020cxcd and other low-mass SN explosions. However, there are no spectropolarimetric observations that have been carried out for SN 2020cxcd. [Pastorello et al. \(2009\)](#) reported that SN 2005cs possesses asymmetric  $H\alpha$  line shapes during the nebular phase with the emission maximum in the P-Cygni profiles shifted towards redder wavelengths by 700–800 km s<sup>-1</sup>. The latter might be explained by an asymmetric distribution of the radioactive material, i.e., by a dominant fraction of the  $^{56}\text{Ni}$  in the inner part of the SN ejecta pointing away from the observer ([Chugai 2006](#)). Moreover, [Gnedin et al. \(2007\)](#) presented imaging polarimetry of SN 2005cs and reported up to 8% polarisation during the plateau phase. Such a high degree of polarisation would be unprecedented for Type II SNe ([Leonard et al. 2002](#)) and might link to an asymmetry in the inner ejecta. Another example of a low-luminosity SN with available spectropolarimetric observations is SN 2008bk. However, the plateau luminosity of this SN is 0.4 dex higher than that of many low-luminosity SNe, whereas its photospheric velocities are comparable to those of other cases of the low-luminosity family ([Pignata 2013](#); [Lisakov et al. 2018](#)). The polarimetric behaviour during the plateau of SN 2008bk is pretty normal and inconspicuous, but after the drop from the plateau this SN retains a constant 0.3% polarisation, which is unusual and might indicate some asymmetry inside

the ejecta ([Leonard et al. 2012](#)). Therefore, although it is not possible to draw solid conclusions about explosion asymmetries on grounds of the existing data sets for SN 2005cs and SN 2020cxcd, a possible role of such asymmetries in low-mass, low-energy, low-luminosity SNe can not be firmly excluded either. This stresses the need of more observational data to be compared with predictions for light curves, spectra, and polarisation based on 3D radiative transfer calculations in 3D explosion models.

#### 4 SUMMARY AND CONCLUSIONS

In this study we compared the observational data of the low-luminosity SNe 2020cxcd and 2005cs with multi-band light curves and photospheric velocities obtained from radiation-hydrodynamics calculations for a 3D explosion model of a  $9.0 M_\odot$  (ZAMS mass) red supergiant progenitor with an iron core of  $1.3 M_\odot$  and a radius of  $408 R_\odot$  ([Woosley & Heger 2015](#)). The stellar model had a pre-collapse mass of  $8.75 M_\odot$  (an ejecta mass of  $7.4 M_\odot$ ) and was self-consistently exploded by the neutrino-driven mechanism in a 3D simulation by [Stockinger et al. \(2020\)](#). The model had developed a considerable asphericity by hydrodynamic instabilities aiding the onset of the explosion. These initial asymmetries ultimately evolved into large-scale asymmetries in the angular distribution of  $^{56}\text{Ni}$ , connected to extended radial mixing of metals from the core into the hydrogen-helium envelope. This mixing proceeded in the form of elongated wide-angle plumes, which led to a prolate global deformation of the chemical composition in the ejecta (see Figure 1 and for details, see [Stockinger et al. 2020](#)).

The subsequent long-time SN evolution, starting from the 3D explosion model at 1.974 days after core bounce, was carried out by spherically symmetric hydrodynamical simulations with the STELLA code, including multi-band radiative transfer. For that we considered the spherically averaged 3D model as well as the conditions in selected radial directions with a different extent of outward metal mixing, covering big  $^{56}\text{Ni}$  plumes as well as regions of less efficient mixing. Performing radiative transfer calculations with the spherically averaged stellar profiles for these selected directions was intended to demonstrate the possible relevance of asymmetry effects in the radiation emission of the 3D explosion model. Aspherical radiation transport can, of course, be reliably treated only by 3D radiative transfer calculations in the 3D SN ejecta, whereas our approach tends to massively overestimate the influence of direction-dependent variations in the density structure and chemical composition. But nevertheless, our calculations might demonstrate the basic trends that could be associated with the existence of such large-scale chemical and density anisotropies in a fully multi-dimensional radiative transfer treatment.

We found that our neutrino-driven explosion model of the  $9 M_\odot$  progenitor with an explosion energy of 0.07 foe and an ejecta mass of  $7.4 M_\odot$  can amazingly well reproduce the basic properties of the bolometric light curve of SN 2020cxcd, i.e., its initial decline to the plateau, the height and duration of the plateau, and the shallow increase of the plateau luminosity until the steep decline to the radioactive-decay tail. This is achieved without any fine tuning of the explosion model except for a proper scaling of the  $^{56}\text{Ni}$  mass to the observationally inferred value of  $0.003 M_\odot$  for SN 2020cxcd. Such a scaling is motivated by considerable modeling uncertainties with respect to an exact determination of the  $^{56}\text{Ni}$  yield. Good overall agreement was also obtained for the broad-band light curves of this SN. In contrast, however, the line velocities reported by [Yang et al. \(2021\)](#) do not mirror the time evolution of the photospheric expan-

sion velocities deduced from our radiative transfer calculations but are considerably higher (up to a factor of  $\sim 3$ ) than the model values. This holds true even in the directions of the fastest ejecta expansion connected to the most extended nickel-rich plume, and even after scaling down the measured  $H\alpha$  line velocities by a factor of 1.4 as recommended by Dessart & Hillier (2005) for comparison with the photospheric velocities from radiative transfer modeling.

This is in stark contrast to our findings for SN 2005cs, which is a template case of a low-energy, low-luminosity SN with low  $^{56}\text{Ni}$  production. Here not only the bolometric and broad-band light curves match the observational ones reasonably well, again without any other tuning than scaling the  $^{56}\text{Ni}$  mass. Also the photospheric velocities are close to the velocities of the  $\text{Sc II}$  line and the down-scaled  $H\alpha$  line of SN 2005cs and follow their evolutionary behavior.

We speculated whether the different shapes of the light curves of SN 2005cs and SN 2020cxid during the initial decline to the plateau and the early plateau phase might be connected to large-scale ejecta asymmetries already at shock breakout and during the early expansion of the outer parts of the hydrogen envelope. Such a possibility is suggested by our 3D explosion model of the  $9 M_{\odot}$  progenitor, which exhibits large-scale asymmetries of the nickel-rich ejecta, which extend through the entire hydrogen envelope and lead to asymmetric shock breakout (see Stockinger et al. 2020 and Figure 1). Contributions by radiation emitted from the faster and more rapidly expanding directions of the ejecta might enhance the luminosity of SN 2005cs before and during the plateau until about 80–90 days, whereas in SN 2020cxid such effects might not play an important role or they might not be visible from our viewing direction. Interestingly, we also witnessed the trend that at early phases the line velocities of SN 2005cs were best compatible with the photospheric velocities in the directions of the fastest ejecta in our aspherical 3D explosion model, whereas with progressing time they approached those of the ejecta in directions with slower expansion, and, at late times, they agreed with those of the angle-averaged ejecta. This might also be interpreted as a possible indication of large-scale or even global explosion asymmetries in the outer ejecta of SN 2005cs, adding to similar conclusions previously drawn by Pastorello et al. (2009), Chugai (2006), and Gnedin et al. (2007) on grounds of asymmetric  $H\alpha$  line shapes and polarisation measurements. A better theoretical understanding of whether such a speculative possibility can explain the light-curve differences of SN 2005cs and SN 2020cxid and the evolution of their line velocities will require 3D radiative transfer calculations for our 3D explosion model or other simulations of asymmetric SNe of low-mass progenitors.

In both of the cases of SN 2020cxid and SN 2005cs, a very low-energy explosion of our low-mass iron-core progenitor can explain the main light-curve features. We reason that the similarities between the photospheric velocities of our model and the line velocities for SN 2005cs and their mismatch in the case of SN 2020cxid point to a considerable overestimation of the observationally inferred line velocities in the latter case. We discussed the corresponding instrumental and diagnostic uncertainties. Both SNe, therefore, seem to comply with the correlation between explosion energy and ejected mass of  $^{56}\text{Ni}$  inferred from Type IIP SN observations (Pejcha & Prieto 2015b; Müller et al. 2017b; Pejcha 2020) and theoretically expected for neutrino-driven explosions (Ertl et al. 2016; Müller et al. 2016; Sukhbold et al. 2016; Ertl et al. 2020).

A striking difference is observed when comparing the explosion energy of our explosion and light-curve model, 0.07 foe, to the explosion energies of low-luminosity SNe derived with the use of the so-called Markov Chain Monte Carlo (MCMC) fitting method (Nagy & Vinkó 2016). For example, SN 2020cxid was reported to

have a total energy of 0.58 foe (Yang et al. 2021), SN 2005cs to have a sum of kinetic and thermal energy of 0.73 foe, and its declared twin PSN J17292918+7542390 (SN-NGC 6412, Jäger et al. 2020) to have an even higher explosion energy of 0.82–0.93 foe. Using the same method, the reference Type IIP SN 1999em was diagnosed to originate from the explosion of a progenitor of about  $20 M_{\odot}$  (the ejecta mass was estimated to be  $19 M_{\odot}$ ) with a diagnostic energy of 4.53 foe. At the same time the recent progress in self-consistent core-collapse explosion simulations coupled with direct radiative transfer hydrodynamics calculations for the light curve has been able to reproduce this SN 1999em by an explosion of a  $15 M_{\odot}$  progenitor with an energy of 0.55 foe (Utrobin et al. 2017). Hence, there is a factor of 10 difference in the derived SN parameters. The MCMC fitting procedure is likely to suffer from various weak points, among them might be a relatively high lower limit for the explosion energy of 0.6 foe (Hamuy 2003) and a simplified method for computing the bolometric light curve (Arnett & Fu 1989; Popov 1993; Nagy et al. 2014). However, the details of the statistical analysis are not fully described in the mentioned references, which complicates any assessment of the employed fitting procedure and results in detail.

## ACKNOWLEDGMENTS

AK is supported by the Alexander von Humboldt Foundation. HTJ and DK acknowledge support by the Deutsche Forschungsgemeinschaft (DFG, German Research Foundation) through Sonderforschungsbereich (Collaborative Research Center) SFB-1258 “Neutrinos and Dark Matter in Astro- and Particle Physics (NDM)” and under Germany’s Excellence Strategy through Cluster of Excellence ORIGINS (EXC-2094)-390783311, and by the European Research Council through Grant ERC-AdG No. 341157-COCO2CASA. AK thanks Stephen Justham, Alexei Mironov and Patrick Neunteufel for fruitful discussions.

## DATA AVAILABILITY

The data computed and analysed for the current study are available via the link <https://www.mpa.mpa-garching.mpg.de/ccsnarchive/>. Results from the core-collapse explosion simulations are accessible for download upon request at the same website.

## REFERENCES

- Arnett W. D., 1980, *ApJ*, 237, 541
- Arnett W. D., Fu A., 1989, *ApJ*, 340, 396
- Blagorodnova N., et al., 2018, *PASP*, 130, 035003
- Blinnikov S. I., Röpke F. K., Sorokina E. I., Gieseler M., Reinecke M., Travaglio C., Hillebrandt W., Stritzinger M., 2006, *A&A*, 453, 229
- Bollig R., Yadav N., Kresse D., Janka H.-T., Müller B., Heger A., 2021, *ApJ*, 915, 28
- Burrows A., Radice D., Vartanyan D., 2019, *MNRAS*, 485, 3153
- Chugai N. N., 2006, *Astronomy Letters*, 32, 739
- Dessart L., Hillier D. J., 2005, *A&A*, 439, 671
- Ertl T., Janka H. T., Woosley S. E., Sukhbold T., Ugliano M., 2016, *ApJ*, 818, 124
- Ertl T., Woosley S. E., Sukhbold T., Janka H. T., 2020, *ApJ*, 890, 51
- Faran T., et al., 2014, *MNRAS*, 442, 844
- Glas R., Just O., Janka H. T., Obergaulinger M., 2019, *ApJ*, 873, 45
- Gnedin Y. N., Larionov V. M., Konstantinova T. S., Kopatskaya E. N., 2007, *Astronomy Letters*, 33, 736
- Goldberg J. A., Bildsten L., Paxton B., 2019, *ApJ*, 879, 3

- Grasberg E. K., Nadezhin D. K., 1976, *Ap&SS*, **44**, 409
- Hamuy M., 2003, *ApJ*, **582**, 905
- Jäger Zoltán J., et al., 2020, *MNRAS*, **496**, 3725
- Janka H.-T., 2017, in Alsabti A. W., Murdin P., eds., *Handbook of Supernovae*. Cham, Switzerland: Springer Nature, p. 1095, doi:10.1007/978-3-319-21846-5\_109
- Jerkstrand A., Ertl T., Janka H. T., Müller E., Sukhbold T., Woosley S. E., 2018, *MNRAS*, **475**, 277
- Kasen D., Woosley S. E., 2009, *ApJ*, **703**, 2205
- Kozyreva A., Nakar E., Waldman R., 2019, *MNRAS*, **483**, 1211
- Kozyreva A., Shingles L., Mironov A., Baklanov P., Blinnikov S., 2020, *MNRAS*, **499**, 4312
- Kozyreva A., Baklanov P., Jones S., Stockinger G., Janka H.-T., 2021, *MNRAS*, **503**, 797
- Lentz E. J., et al., 2015, *ApJ*, **807**, L31
- Leonard D. C., Filippenko A. V., Chornock R., Li W., 2002, *AJ*, **124**, 2506
- Leonard D. C., Dessart L., Hillier D. J., Pignata G., 2012, in Hoffman J. L., Bjorkman J., Whitney B., eds., *American Institute of Physics Conference Series Vol. 1429, Stellar Polarimetry: from Birth to Death*. pp 204–207 (arXiv:1109.5406), doi:10.1063/1.3701926
- Levesque E. M., Massey P., Olsen K. A. G., Plez B., Josselin E., Maeder A., Meynet G., 2005, *ApJ*, **628**, 973
- Levesque E. M., Massey P., Olsen K. A. G., Plez B., Meynet G., Maeder A., 2006, *ApJ*, **645**, 1102
- Lisakov S. M., Dessart L., Hillier D. J., Waldman R., Livne E., 2018, *MNRAS*, **473**, 3863
- Mattila S., Smartt S. J., Eldridge J. J., Maund J. R., Crockett R. M., Danziger I. J., 2008, *ApJ*, **688**, L91
- Melson T., Janka H.-T., Marek A., 2015a, *ApJ*, **801**, L24
- Melson T., Janka H.-T., Bollig R., Hanke F., Marek A., Müller B., 2015b, *ApJ*, **808**, L42
- Melson T., Kresse D., Janka H.-T., 2020, *ApJ*, **891**, 27
- Moriya T. J., Suzuki A., Takiwaki T., Pan Y.-C., Blinnikov S. I., 2020, *MNRAS*, **497**, 1619
- Müller B., Heger A., Liptai D., Cameron J. B., 2016, *MNRAS*, **460**, 742
- Müller B., Melson T., Heger A., Janka H.-T., 2017a, *MNRAS*, **472**, 491
- Müller T., Prieto J. L., Pejcha O., Clocchiatti A., 2017b, *ApJ*, **841**, 127
- Müller B., Gay D. W., Heger A., Tauris T. M., Sim S. A., 2018, *MNRAS*, **479**, 3675
- Nagy A. P., Vinkó J., 2016, *A&A*, **589**, A53
- Nagy A. P., Ordasi A., Vinkó J., Wheeler J. C., 2014, *A&A*, **571**, A77
- Nakamura K., Takiwaki T., Kuroda T., Kotake K., 2015, *PASJ*, **67**, 107
- O'Connor E., Ott C. D., 2011, *ApJ*, **730**, 70
- Ott C. D., Roberts L. F., da Silva Schneider A., Fedrow J. M., Haas R., Schnetter E., 2018, *ApJ*, **855**, L3
- Pastorello A., et al., 2006, *MNRAS*, **370**, 1752
- Pastorello A., et al., 2009, *MNRAS*, **394**, 2266
- Pejcha O., 2020, in Kabáth P., Jones D., Skarka M., eds., *Reviews in Frontiers of Modern Astrophysics; From Space Debris to Cosmology*. Cham, Switzerland: Springer Nature, pp 189–211, doi:10.1007/978-3-030-38509-5\_7
- Pejcha O., Prieto J. L., 2015a, *ApJ*, **799**, 215
- Pejcha O., Prieto J. L., 2015b, *ApJ*, **806**, 225
- Pignata G., 2013, in *Massive Stars: From alpha to Omega*. p. 176
- Popov D. V., 1993, *ApJ*, **414**, 712
- Pumo M. L., Zampieri L., Spiro S., Pastorello A., Benetti S., Cappellaro E., Manicò G., Turatto M., 2017, *MNRAS*, **464**, 3013
- Reguitti A., et al., 2021, *MNRAS*, **501**, 1059
- Spiro S., et al., 2014, *MNRAS*, **439**, 2873
- Stockinger G., et al., 2020, *MNRAS*, **496**, 2039
- Sukhbold T., Ertl T., Woosley S. E., Brown J. M., Janka H.-T., 2016, *ApJ*, **821**, 38
- Summa A., Janka H.-T., Melson T., Marek A., 2018, *ApJ*, **852**, 28
- Takiwaki T., Kotake K., Suwa Y., 2014, *ApJ*, **786**, 83
- Tomasella L., et al., 2018, *MNRAS*, **475**, 1937
- Tsvetkov D. Y., Volnova A. A., Shulga A. P., Korotkiy S. A., Elmhamdi A., Danziger I. J., Ershko M. V., 2006, *A&A*, **460**, 769
- Utrobin V. P., Chugai N. N., 2008, *A&A*, **491**, 507
- Utrobin V. P., Wongwathanarat A., Janka H.-T., Müller E., 2017, *ApJ*, **846**, 37
- Van Dyk S. D., et al., 2012, *AJ*, **143**, 19
- Weaver T. A., Zimmerman G. B., Woosley S. E., 1978, *ApJ*, **225**, 1021
- Woosley S. E., Heger A., 2015, *ApJ*, **810**, 34
- Yang S., et al., 2021, *A&A*, **655**, A90

## APPENDIX A: PROFILES OF THE ANGLE-AVERAGED EXPLOSION-MODEL DATA USED IN KOZYREVA ET AL. (2021) AND IN THE PRESENT STUDY

We show the employed initial profiles of the angle-averaged density, velocity, and  $^{56}\text{Ni}$  mass fraction versus radius (Figure A1) and enclosed mass (Figure A2) compared to the profiles used in Kozyreva et al. (2021).

## APPENDIX B: ANGLE-AVERAGED AND RADIAL-DIRECTION DEPENDENT PROFILES EXTRACTED FROM THE 3D SUPERNOVA EXPLOSION SIMULATION

We show the density,  $^{56}\text{Ni}$  mass fraction, and velocity profiles of all selected radial directions as initial data for the radiation-hydrodynamics simulations in the present study in Figure B1, Figure B2, and Figure B3, respectively. It is seen that at the given time of 1.97 days after core collapse, the shock wave in the fastest moving part of the SN ejecta in model s9.0, which corresponds to the directions  $0^\circ - 10^\circ$ , is within about  $3 \times 10^{12}$  cm from the stellar surface, and breaks out within  $\sim 0.2$  days. The shock wave in the slowest part of the ejecta is still about  $10^{13}$  cm away from the stellar edge and will reach the surface roughly 1 day after the fastest regions of the shock.

## APPENDIX C: BROAD-BAND LIGHT CURVES FOR ALL RADIAL DIRECTIONS IN THE PRESENT STUDY

We present the *UBVR* broad-band magnitudes for all radial directions considered in our study and the angle-averaged profile of model s9.0 in Figure C1.

This paper has been typeset from a  $\text{\TeX}/\text{\LaTeX}$  file prepared by the author.

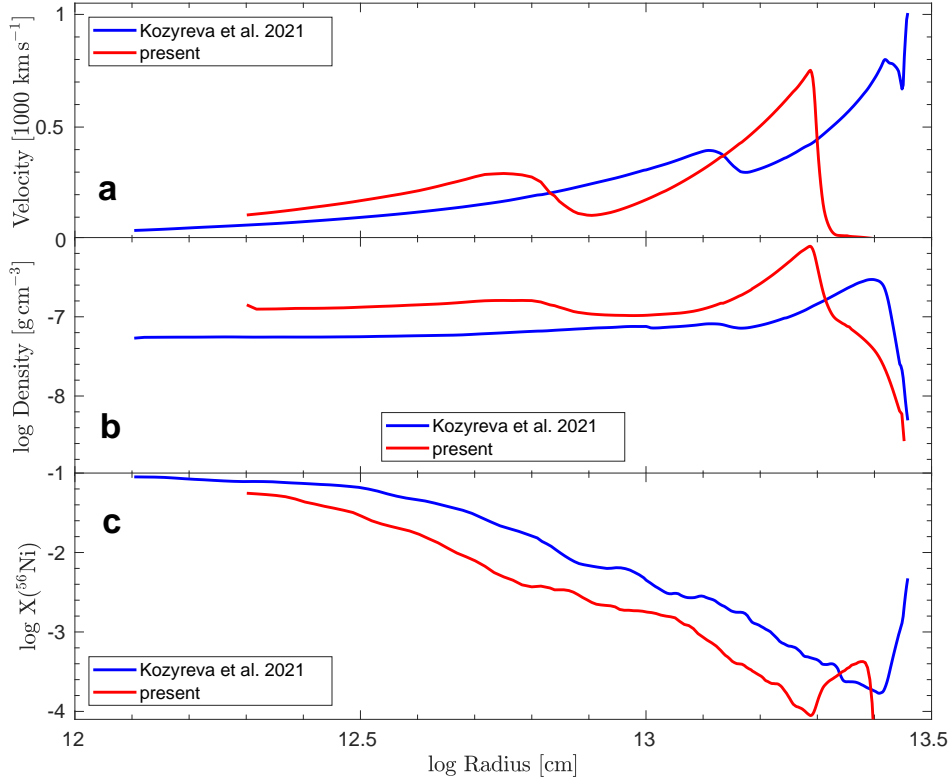


**Figure A1.** Velocity (a), density (b) and <sup>56</sup>Ni mass fraction (c) of the angle-averaged profiles used in the present study and in Kozyreva et al. (2021) along the radius coordinate

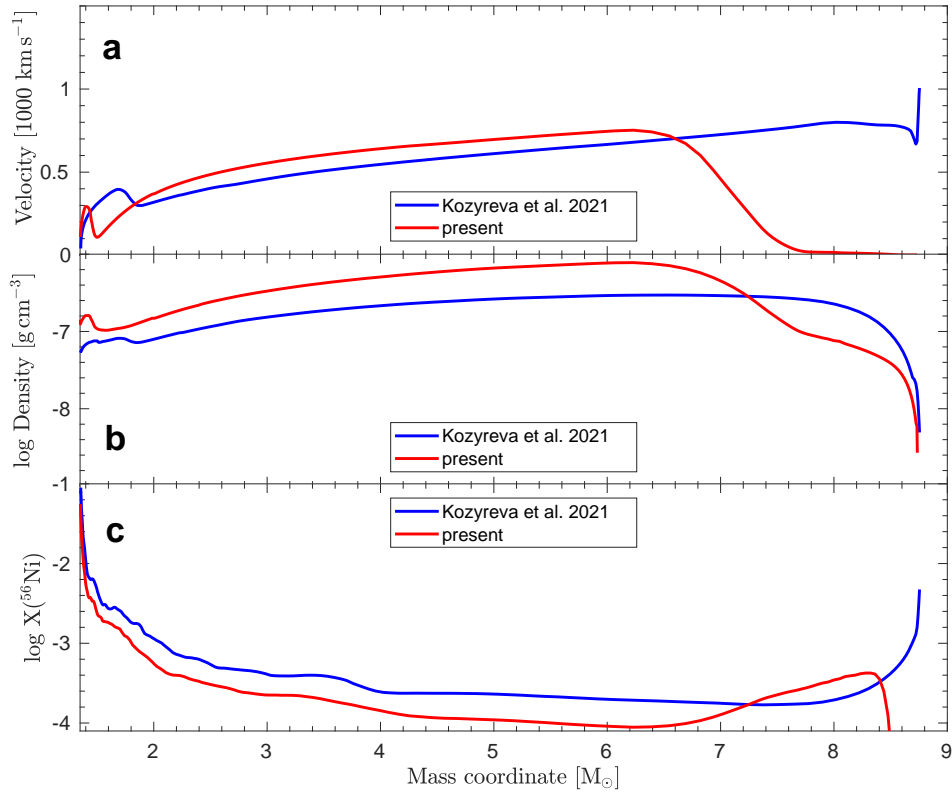


**Figure A2.** Velocity (a), density (b) and <sup>56</sup>Ni mass fraction (c) of the angle-averaged profiles used in the present study and in Kozyreva et al. (2021) along the mass coordinate.

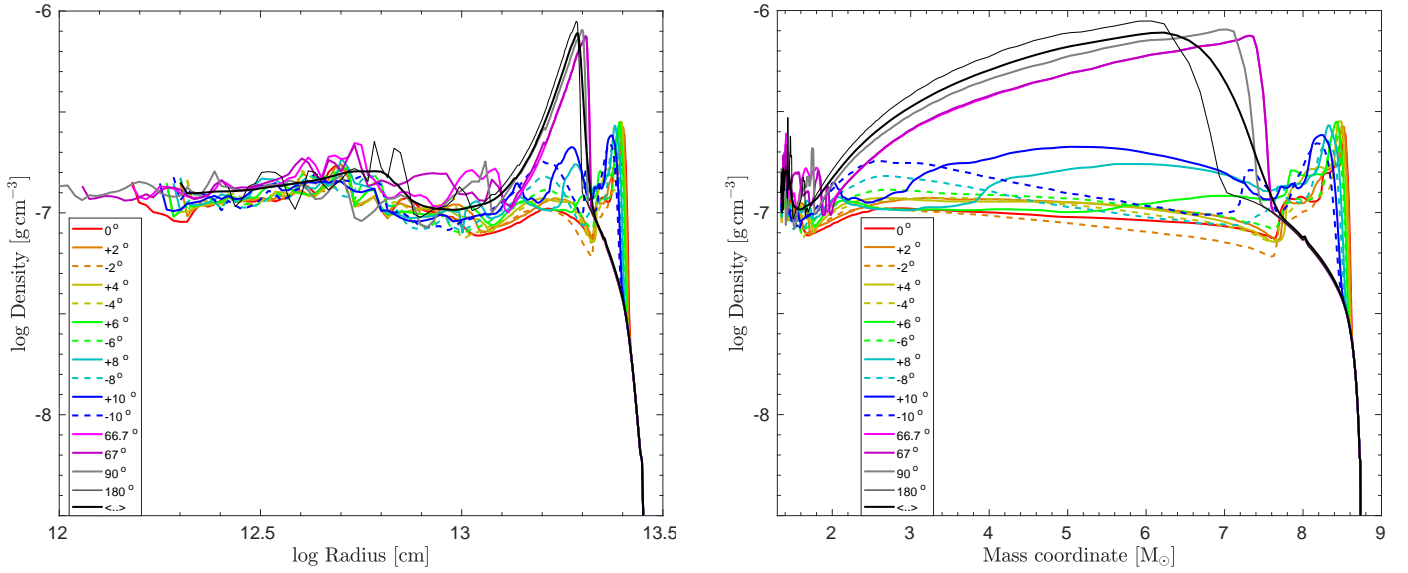


**Figure B1.** Density of the angle-averaged profile (“< .. >”) and different radial directions of the model s9.0 used in the present study along the radius coordinate (left) and the mass coordinate (right).

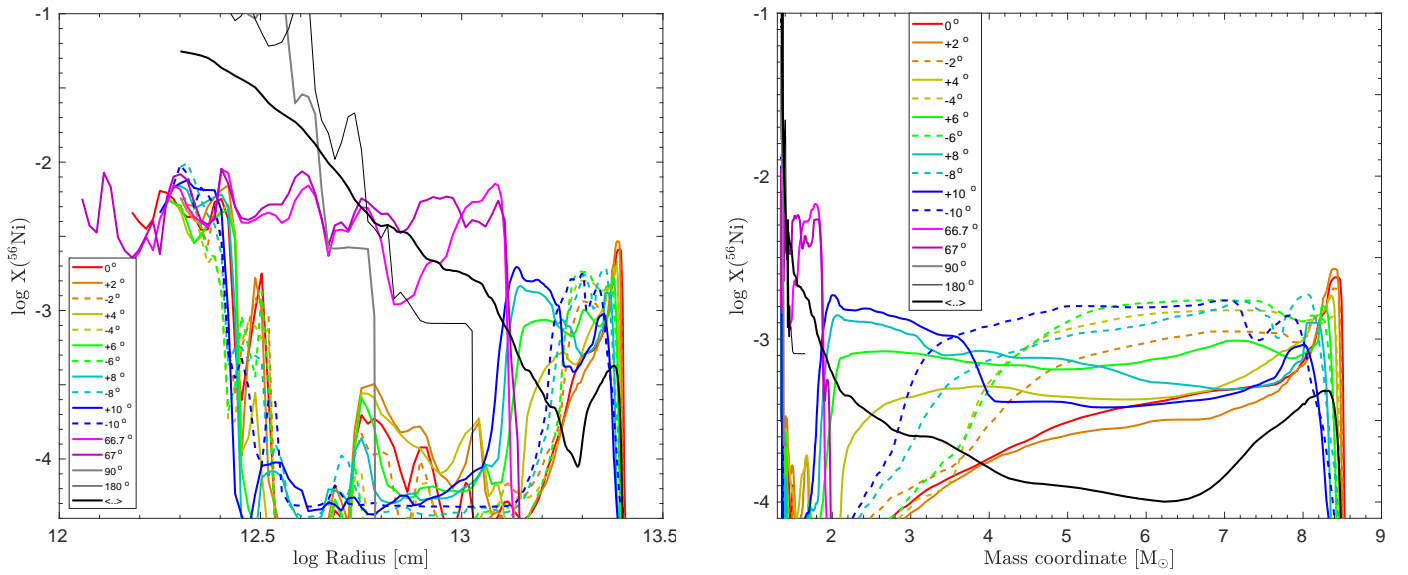


**Figure B2.**  $^{56}\text{Ni}$  mass fraction of the angle-averaged profile (“< .. >”) and different radial directions of the model s9.0 used in the present study along the radius coordinate (left) and the mass coordinate (right).

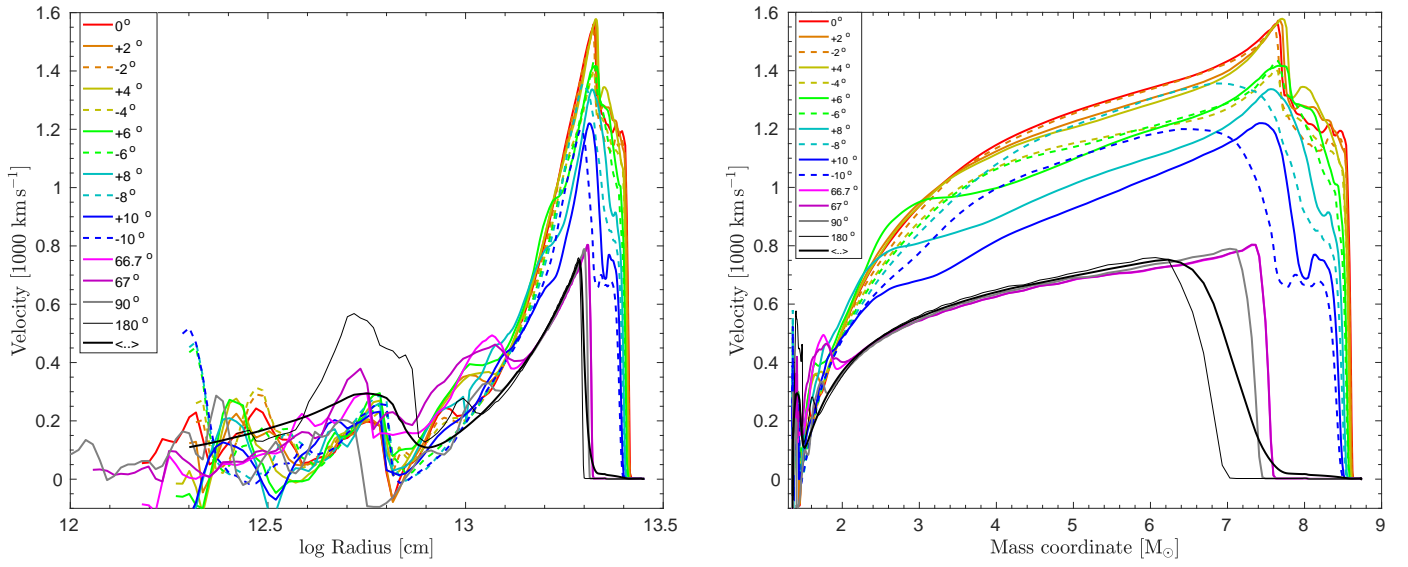


**Figure B3.** Velocity of the angle-averaged profile (“< .. >”) and different radial directions of the model s9.0 used in the present study along the radius coordinate (left) and the mass coordinate (right).

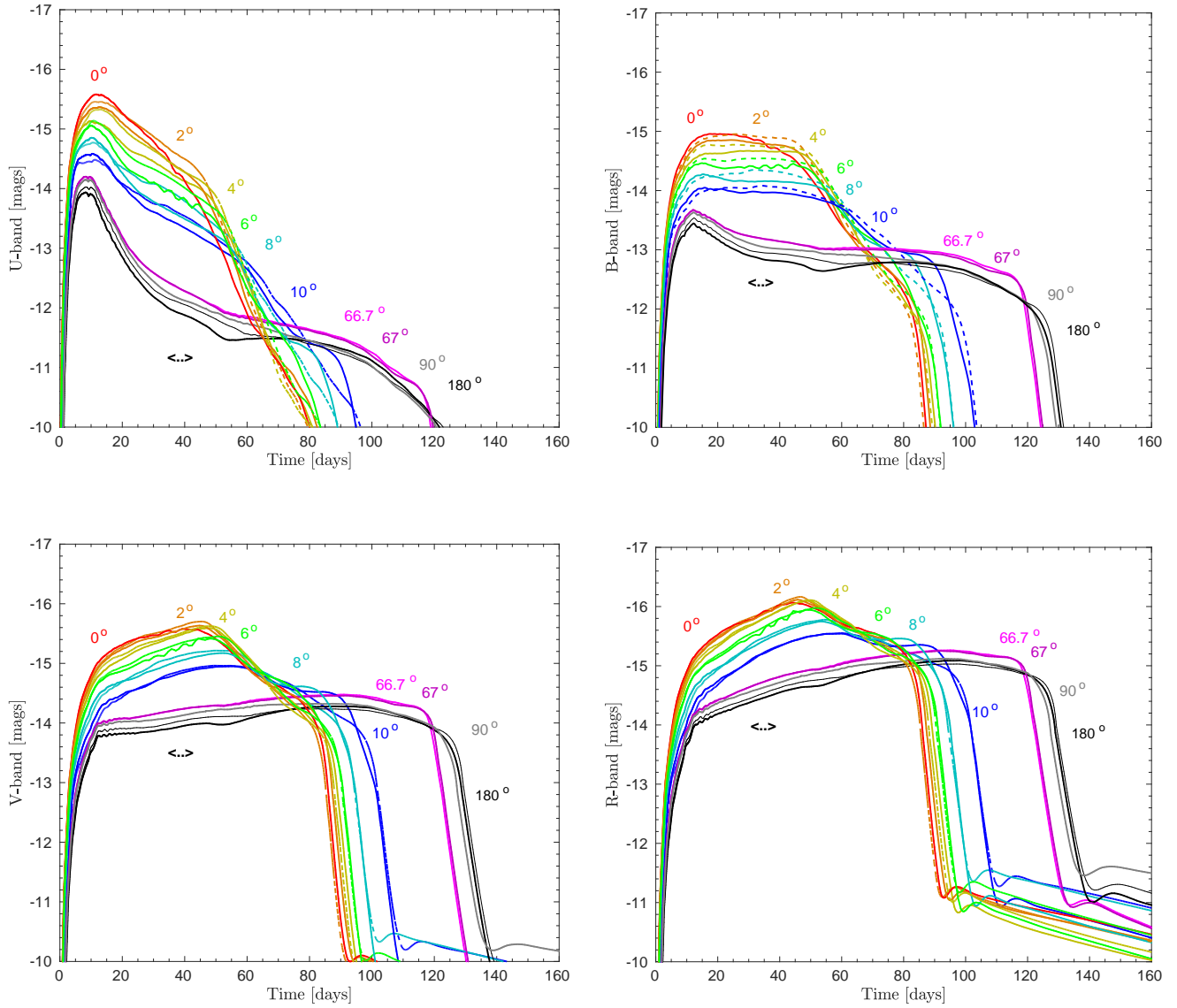


**Figure C1.** *UBVR* broad-band light curves for the angle-averaged profile (“<..>”) and different radial directions of the 3D model s9.0. The solid and dashed curves indicate the “+” and “-” directions for the cases of 2°–10°, as introduced in Table 2.